Prediction of transport, deposition, and resultant immune response of nasal spray vaccine droplets using a CFPD–HCD model in a 6-year-old upper airway geometry to potentially prevent COVID-19

Hamideh Hayati[1], Yu Feng[1] (✉), Xiaole Chen[2], Emily Kolewe[3], Catherine Fromen[3]

1. School of Chemical Engineering, Oklahoma State University, Stillwater, OK 74078, USA
2. School of Energy and Mechanical Engineering, Nanjing Normal University, Nanjing 210042, China
3. Department of Chemical and Biomolecular Engineering, University of Delaware, Newark, DE 19716, USA

Abstract

This study focuses on the transport, deposition, and triggered immune response of intranasal vaccine droplets to the angiotensin-converting-enzyme-2-rich region, i.e., the olfactory region (OR), in the nasal cavity of a 6-year-old female to possibly prevent corona virus disease 19 (COVID-19). To investigate how administration strategy can influence nasal vaccine efficiency, a validated multi-scale model, i.e., computational fluid–particle dynamics (CFPD) and host-cell dynamics (HCD) model, was employed. Droplet deposition fraction, size change, residence time, and the area percentage of OR covered by the vaccine droplets, and triggered immune system response were predicted with different spray cone angles, initial droplet velocities, and compositions. Numerical results indicate that droplet initial velocity and composition have negligible influences on the vaccine delivery efficiency to OR. In contrast, the spray cone angle can significantly impact the vaccine delivery efficiency. The triggered immunity was not significantly influenced by the administration investigated in this study due to the low percentage of OR area covered by the droplets. To enhance the effectiveness of the intranasal vaccine to prevent COVID-19 infection, it is necessary to optimize the vaccine formulation and administration strategy so that the vaccine droplets can cover more epithelial cells in OR to minimize the number of available receptors for SARS-CoV-2.

1 Introduction

Intranasal vaccination against corona virus disease 19 (COVID-19) caused by SARS-CoV-2 could be highly advantageous over conventional intramuscular vaccination. Indeed, the nasal cavity is the initial site of viral infection, replication, and transmission (Chen et al., 2020; Chavda et al., 2021; Pilicheva and Boyuklieva, 2021; Xi et al., 2021). After virus-laden droplets enter the nasal cavity, the spike protein (S) on their surface binds to the angiotensin-converting enzyme 2 (ACE-2) receptor found in abundance in the olfactory region (OR) (Chen et al., 2020; Chavda et al., 2021; Pilicheva and Boyuklieva, 2021). This might be the reason for the loss of olfaction among COVID-19 patients and suggests intranasal therapy.

Intranasal vaccines seem promising because they function similarly to viral infection. Additionally, they can be conveniently and painlessly self-administered (Chavda et al., 2021). From the immunology perspective, intranasal vaccines trigger both mucosal and systemic immune responses (Krammer, 2020; Chavda et al., 2021). Experimental studies demonstrate that neutralizing SARS-CoV-2-specific mucosal immunoglobulin A (IgA) antibodies could vanish the infection (Butler et al., 2021; Chavda et al., 2021). However, usually intramuscular vaccines can only trigger robust immunoglobulin G (IgG) response in the lower respiratory tract, but cannot lead to adequate mucosal IgA response in the upper respiratory tract. Therefore, systemically vaccinated individuals are still susceptible to asymptomatic viral infection and can transmit the live virus to others (Bleier et al., 2021).

✉ yu.feng@okstate.edu

Nomenclature

A_d	droplet surface area (m²)
C_m	correction factor for Fuchs–Knudsen number
c_P	specific heat of humid air (J/(kg·K))
$c_{P,d}$	specific heat of droplet (J/(kg·K))
D_w	water mass diffusivity (m²/s)
d_d	droplet diameter (m)
$d_{d,i}$	droplet initial diameter (m)
$d_{d,f}$	droplet final diameter (m)
E_0	initial number of epithelial cells
$\vec{F}^{BM}$	Brownian motion induced force (N)
$\vec{F}^{D}$	drag force (N)
$\vec{F}^{G}$	gravity (N)
$\vec{F}^{L}$	Saffman lift force (N)
$\vec{g}$	gravitational acceleration (m/s²)
H_{lat}	latent heat (J/kg)
K_w	Kelvin effect factor
Kn	Knudsen number
k	turbulence kinetic energy (J/kg)
k_c	thermal conductivity (W/(m·K))
$k_{c,t}$	turbulent thermal conductivity (W/(m·K))
k_{hc}	modified thermal conductivity (W/(m²·K))
k_{mc}	mass transfer coefficient (m/s)
M_w	water molecular weight (kmol/kg)
m_d	droplet mass (kg)
N	number of fragments between max and min temperature
Nu	Nusselt number
P_{eq}	equilibrium vapor pressure (Pa)
P_{sat}	saturation vapor pressure (Pa)
Pr	Prandtl number
R	gas constant (J/(mol·K))
Re_d	droplet Reynolds number
r_d	droplet radius (m)
S_w^m	mass source term (kg/(m³·s))
Sc	Schmidt number
Sh	Sherwood number
T	humid airflow temperature (K)
T_d	droplet temperature (K)
t	time (s)
$\vec{u}$	flow velocity (m/s)
$\vec{u}_d$	droplet velocity (m/s)
V	breathing velocity (m/s)
$V_{d,i}$	droplet initial velocity (m/s)
$\bar{V}_w$	water molar volume (m³/kmol)
$y_{w,surf}$	water mass fraction at droplet surface
$y_{w,\infty}$	water mass fraction in humid air mixture

Greek symbols

α_m	mass accommodation factor
λ	gas mixture mean free path (m)
μ	viscosity of humid air (kg/(m·s))
μ_t	turbulent viscosity of humid air (kg/(m·s))
$\mu_{d,surf}$	viscosity of humid air at droplet surface (kg/(m·s))
ρ	density of humid airflow (kg/m³)
ρ_w	density of water (kg/m³)
σ	droplet surface tension (N/m)
τ	breathing cycle time (s)
Φ_{exp}	experimental values of reported immune response
Φ_{HCD}	computational values obtained for immune response
ω	specific rate of turbulence kinetic energy dissipation (J/(kg·s))

Acronyms

λ-C	λ-carrageenan
ACE-2	angiotensin-converting enzyme 2
CFPD	computational fluid–particle dynamics
COVID-19	corona virus disease 2019
DF	deposition fraction
G	generation
GG	gellan gum
HCD	host-cell dynamics
IgA	immunoglobulin A
IgG	immunoglobulin G
MRI	magnetic resonance imaging
NK	natural killer cells
ODEs	ordinary differential equations
OR	olfactory region
PBS	phosphate-buffered saline
RH	relative humidity
RMSE	root mean squared error
S	spike protein
SARS-CoV-2	severe acute respiratory syndrome corona virus 2
SST	shear stress transport
TB	tracheobronchial
UDFs	user-defined functions
VC	vaccine coverage
VT_0	initial viral titer

Hence, nasal spray delivery of SARS-CoV-2 vaccine candidates to ACE-2-rich areas can be substantially effective in preventing COVID-19 infection and transmission (Xi et al., 2021).

Other than the benefits mentioned above for intranasal vaccines, they can also benefit individuals and children who are afraid of needles (Chavda et al., 2021). It was reported (Flaherty, 2021) that children and adolescents could be dangerous carriers and spreaders of COVID-19 due to their capability of carrying high levels of SARS-CoV-2 in their respiratory secretion. Preventing SARS-CoV-2 transmission and infection among them will be highly beneficial for community immunity (Glezen, 2001). Therefore, it is necessary to investigate how intranasal vaccine transports and triggers the immune system response in the pulmonary routes of children.

To administer intranasal vaccines with desired effectiveness, some factors need to be fine-tuned. Among all the factors mentioned in the literature (Xi et al., 2021), nasal ACE-2-rich locations as the targeted delivery sites, the type of nasal spray device, delivery strategy, nasal physiology, and inter-subject variability are possibly the main factors in determining the vaccination effectiveness. Specifically, ACE-2-rich areas in the nasal cavity should be the target site for vaccine delivery. However, the complex morphology of the nasal passage makes it challenging for the vaccine droplets to reach the targeted area. In addition, inter-subject variability of the nasal cavity anatomy between different age groups (e.g., adults vs. children) can significantly influence the transport and deposition of inhaled nasal spray droplets. Therefore, assessment of nasal vaccine delivery for children using their age-specific nasal cavity geometries is necessary since it will be able to avoid biased conclusions drawn from the research results obtained using adult nasal cavity geometries.

As of December 2021, there have been some nasal vaccine sprays in phase-1 clinical trials against SARS-CoV-2 (Hassan et al., 2020). A fully preventative spray (Moakes et al., 2021) was formulated to target the lining of the upper respiratory system against SARS-CoV-2 as an intranasal vaccine potential candidate. It is a polysaccharide-based spray, of which the physical properties such as spray droplet size distribution and antiviral properties were documented. In detail, gellan gum (GG) and λ-carrageenan (λ-C) are two biocompatible and intrinsically muco-adhesive components of vaccine solution. Their high viscosity can reduce the clearance due to dripping, thereby enhancing spray residence time in the nasal cavity (Moakes et al., 2021). It has also been claimed that GG and λ-C demonstrate antiviral capacities. Phosphate-buffered saline (PBS) was added to the vaccine solution because of its buffering capacity against GG and λ-C native acid pH. It is possible to deliver the preventative spray (Moakes et al., 2021) as the intranasal vaccine to the

OR to cover more epithelial cells and minimize the number of available receptors for SARS-CoV-2.

There have been many computational fluid–particle dynamics (CFPD) studies elucidating the transport dynamics of spray particles/droplets in the nasal cavity in the past two decades, focusing on the targeted drug delivery to the OR and other regions in the main nasal airway passage. Inthavong et al. (2006, 2008) and Tong et al. (2016) investigated the delivery of nasal spray particles (with selective sizes) into the nasal cavity of a 25-year-old male. The above-mentioned papers investigated particle deposition in the main passage of the nasal cavity, but did not target OR. Kiaee et al. (2018) studied nasal spray particle transport in seven realistic adult nasal airway geometries. Based on their outcomes, nasal spray particle penetration through the nasal cavity is highly sensitive to particle size. They found that the particles of 20–30 μm in diameter are preferred since their deposition in OR is the highest. Calmet et al. (2019) simulated nasal spray particle deposition in a human nasal cavity under multiple inhalation conditions. They claimed that spray deposition in OR is negligible and unaffected by the spray particle conditions, i.e., spray cone angle, insertion angle, and initial velocity. Zare et al. (2022) studied drug delivery to the inferior meatus of the nasal airway model of a 42-year-old female using a spray device with an angled tip. Drug particles were found to be more efficiently guided toward the target area. None of the computational efforts mentioned above have focused on aerosolized COVID-19 vaccine candidates or systematically investigated how administration strategies can influence the deposition of vaccine droplets in the nasal cavity of a young child with realistic relative humidity (RH) and temperature distribution. Additionally, although there are research efforts on modeling SARS-CoV-2 induced immune system responses (Li et al., 2021; Vaidya et al., 2021), dynamics of both innate and adaptive immune system responses against SARS-CoV-2 have not been modeled.

Therefore, focusing on children, this study predicted transport, deposition, and the immune system response of COVID-19 nasal vaccine spray droplets in an upper airway model of a 6-year-old child covering from the nasal cavity to generation 5 (G5) using a multi-scale numerical model, i.e., CFPD–HCD model. The CFPD–HCD model is experimentally calibrated and validated. The transport and deposition of polydisperse COVID-19 nasal vaccine multi-component droplets with initial diameters ranging from 20 to 300 μm were simulated using an experimentally validated CFPD model, which also considered the evaporation/condensation effect on the droplet size change. The vaccine solution consists of water, PBS, GG, and λ-C (Moakes et al., 2021). Parameters that can influence the delivery efficiency of the intranasal COVID-19 vaccine to the targeted

ACE-2-rich region, i.e., the OR, were determined based on the numerical simulation results reported in the literature (Kiaee et al., 2018; Xi et al., 2021). Those parameters include spray cone angle, spray droplet initial velocity, and initial droplet composition. Furthermore, the vaccine droplet deposition data were converted as the initial conditions for the HCD model to predict the variations in immune system responses based on different intranasal administration strategies for the COVID-19 nasal spray vaccine. For this purpose, vaccine coverage (VC) was calculated, which is defined as the percentage of epithelial cells in OR that can be covered by vaccine droplets. Based on the VC value, epithelial cell counts that are susceptible to infection were obtained and introduced to the HCD model. In the present HCD model, the kinetics of macrophages and natural killer (NK) kinetics were appended to the model introduced by Lee et al. (2009).

2 Governing equations

2.1 CFPD model

An experimentally validated CFPD model based on the one-way coupled Euler–Lagrange method was used to simulate multi-component droplet transport in the respiratory system model (Hayati et al., 2021). It was assumed that the droplets are spherical, and droplet–droplet interaction was neglected. Droplets are composed of water, GG, λ-G, and PBS (Moakes et al., 2021). Water is the only evaporable component. Nasal mucosa was not explicitly modeled as a separate fluid phase in this study. Instead, the 100% trapped wall boundary condition was applied, assuming that droplets will deposit when touching the airway walls.

2.1.1 Humid airflow

Since the airflow regime in the respiratory system model was transitional between laminar and turbulence, the transition shear stress transport (SST) (Menter et al., 2006) model was employed to accurately capture the laminar-to-turbulent transition sites. The conservation laws of mass, momentum, and energy, turbulence kinetic energy (k), and the specific rate of dissipation (ω) were provided in previous studies (Haghnegahdar et al., 2019). The convection–diffusion equation (Bird et al., 1960) is employed for the calculation of water vapor (y_w) distribution to predict droplet size change dynamics, i.e.,

$$\frac{\partial(\rho y_w)}{\partial t} + \frac{\partial(\rho u_i y_w)}{\partial x_j} = -\frac{\partial}{\partial x_j}\left[\left(\rho D_w + \frac{\mu_t}{Sc_t}\right)\frac{\partial y_w}{\partial x_j}\right] + S_w^m \quad (1)$$

In this study, air and water vapor are the constituents of the gas mixture. Accordingly, ρ is the density of the mixture,

D_w is the molecular diffusivity of water in air, μ_t is the turbulent viscosity, and S_w^m is the mass source term (i.e., the evaporation rate of water between humid air and droplet).

The energy equation (Longest and Xi, 2008) was solved to predict the temperature distribution in the computational domain, i.e.,

$$\frac{\partial(\rho c_p T)}{\partial t} + \frac{\partial(\rho u_i c_p T)}{\partial x_j}$$
$$= \frac{\partial}{\partial x_j}\left[(k_c + k_{c,t})\frac{\partial T}{\partial x_j} + h\left(\rho D_w + \frac{\mu_t}{Sc_t}\right)\frac{\partial y_w}{\partial x_j}\right] \quad (2)$$

where c_p, T, k_c, and $k_{c,t}$ are the specific heat of the gas mixture, temperature, thermal conductivity, and turbulent thermal conductivity, respectively. In addition, h is the convective heat transfer coefficient of water. Please refer to Hayati et al. (2021) for more details on the governing equations.

2.1.2 Multi-component droplet transport

Droplets traveling along with fluid flow are subjected to multiple forces. To obtain the droplet trajectories, Newton's Second Law was applied (Hayati et al., 2019, 2021), i.e.,

$$\frac{\mathrm{d}}{\mathrm{d}t}(m_d \vec{u}_d) = \vec{F}^D + \vec{F}^L + \vec{F}^{BM} + \vec{F}^G \quad (3)$$

where m_d is the droplet mass, $\vec{u}_d$ is the droplet velocity, $\vec{F}^D$ is the drag force (Chen et al., 2017), $\vec{F}^L$ is the Saffman lift force (Saffman, 1965), $\vec{F}^{BM}$ is the Brownian motion induced force (Hayati et al., 2019), and $\vec{F}^G$ is gravity.

Droplet mass and energy balance equations are employed to calculate the size change induced by evaporation and condensation. The mass balance equation for droplets can be given as

$$\frac{\mathrm{d}m_d}{\mathrm{d}t} = -\bar{n}_w \cdot A_d \quad (4)$$

where A_d is the droplet surface area, and $\bar{n}_w$ is the average mass flux of water evaporation/condensation on the droplet surface, which can be defined by

$$\bar{n}_w = \frac{Sh D_w C_m}{d_d}\ln\left(\frac{1 - y_{w,\infty}}{1 - y_{w,surf}}\right) \quad (5)$$

In Eq. (5), $y_{w,\infty}$ and $y_{w,surf}$ are the mass fractions of water in the vapor phase and at the surface of droplet, respectively. D_w is the mass diffusivity of water, Sh is the Sherwood number (Whitaker, 1972), and C_m is the Fuchs–Knudsen correction factor (Chen et al., 2017).

The Sherwood number (Sh) can be calculated by

$$Sh = 2 + (0.4Re_d^{1/2} + 0.06Re_d^{2/3})Sc^{0.4}\left(\frac{\mu}{\mu_{d,surf}}\right)^{1/4} \quad (6)$$

where $Sc = \mu/(\rho D_e)$ is the Schmidt number, Re_d is the droplet Reynolds number, μ and $\mu_{d,surf}$ are gas mixture viscosities in the fluid and on the droplet surface, respectively. This study assumes $\mu/\mu_{d,surf} = 1$ (Whitaker, 1972).

Furthermore, C_m can be given as

$$C_m = \frac{1 + Kn}{1 + \left(\dfrac{4}{3\alpha_m} + 0.377 \right)Kn + \dfrac{4}{3\alpha_m}Kn^2} \tag{7}$$

where Kn is the Knudsen number, and $\alpha_m = 1$ is the mass accommodation factor (Broday and Georgopoulos, 2001).

It is worth mentioning that the Kelvin effect was taken into account when calculating the water mass fraction $y_{w,surf}$ at the saturated droplet surface in Eq. (5). Specifically, compared with flat liquid surface, the droplet surface curvature allows water molecules to evaporate more freely and faster. Such a phenomenon, i.e., the Kelvin effect, causes the equilibrium vapor pressure to be higher than the saturation vapor pressure at the droplet surface (Brechtel and Kreidenweis, 2000; Asgharian, 2004). Therefore, the Kelvin effect factor K_w can be defined and calculated by

$$K_w = \frac{P_{eq}}{P_{sat}} = \exp\left(\frac{4\sigma \overline{V}_w}{d_d T_d R} \right) \tag{8}$$

Here, P_{sat} is the saturation vapor pressure at droplet temperature and P_{eq} is the equilibrium vapor pressure above the droplet. σ denotes droplet surface tension, $R = 8.314$ J/(mol·K) is the gas constant, and $\overline{V}_w$ is the molar volume of evaporable component, which is defined by (Brechtel and Kreidenweis, 2000):

$$\overline{V}_w = \frac{M_w}{\rho_w} \tag{9}$$

where M_w and ρ_w are the molecular weight and density (Kreidenweis et al., 2005) of water, respectively. Therefore, $y_{w,surf}$ should be calculated by

$$y_{w,surf} = K_w \frac{P_{sat}}{RT_d} \tag{10}$$

The energy balance equation for droplets can be given as

$$\frac{dT_d}{dt} = \left[k_{hc} A_d (T - T_d) - \frac{dm_d}{dt} H_{lat} \right] / (m_d c_{p,d}) \tag{11}$$

where H_{lat} is the latent heat. T_d and $c_{p,d}$ are the droplet temperature and specific heat, respectively. k_{hc} denotes the modified thermal conductivity, which can be calculated by

$$k_{hc} = k_{mc} \frac{Nu k_c}{Sh D_w} \tag{12}$$

In Eq. (12), k_c is the thermal activity of humid air, Nu is the Nusselt number, and $k_{mc} = C_m D_w Sh/d_d$ is the mass transfer coefficient. Assuming there is no internal resistance to heat transfer inside the droplet, Nu can be defined by (Whitaker, 1972):

$$Nu = 2 + (0.4Re_d^{1/2} + 0.06Re_d^{2/3})Pr^{0.4}\left(\mu/\mu_{d,surf} \right)^{1/4} \tag{13}$$

2.2 HCD model

In this study, a two-compartment modeling framework system (i.e., a lung compartment and a lymphatic compartment) of 24 coupled nonlinear stiff ordinary differential equations (ODEs) introduced by Lee et al. (2009) is developed and revised to model the immune system response. The HCD model includes parameters representing the rates at which the viral titer, epithelial cells, and immune cell counts vary. Specifically, viral titer, epithelial cells, interferons, macrophages, NK cells, and dendritic cells are modeled and studied under the lung compartment. Virus-loaded dendritic cells, T cells, B cells, effector cells, and antibodies are simulated and analyzed as the lymphatic compartment. The role of the adaptive effector cells and antibodies are considered in mitigating infected cells and viral load in the lung compartment, respectively. The ODEs of the HCD model and more details can be found in the Appendix. Compared with existing HCD models for SARS-CoV-2 study (Li et al., 2021; Vaidya et al., 2021), the HCD model developed and employed in this study is more advanced since it includes the kinetics of both innate (macrophages, NK cells, interferons, and dendritic cells) and adaptive (CD8^{+} T cells, short-lived, and long-lived antibodies) immune system responses.

3 Initial and boundary conditions

To use the realistic temperature and RH initial conditions inside the respiratory system model before intranasal vaccine spray administration, one breathing cycle was simulated to obtain the temperature and water vapor mass fraction distributions. Details of the boundary conditions are listed in Table 1. Temperature and humidity distribution at airway walls were adopted from Ferron et al. (2013) for the one-breathing cycle simulations before vaccine administration. Vaccine droplets were sprayed into the nasal cavity once the exhalation phase ended.

Since patients usually do not breathe when spraying, the airflow inlet velocity is assumed to be zero when injecting vaccine droplets. Droplet properties and compositions (Moakes et al., 2021) are presented in Table 2.

Initial conditions for HCD model calibration are mentioned

Table 1 Airflow properties and boundary conditions

Inhaled humid airflow properties	
T (K)	RH
298.15	40%

Boundary conditions			
Boundary	T (K)	RH (H$_2$O vapor mass fraction)	BC type
Nostrils	298.15	40%	Velocity inlet[1]
Walls — Nasal cavity	300.15	75% (1.66×10^{-2})	No slip
Pharynx	302.15	75% (1.86×10^{-2})	
Oral cavity	302.15	75% (1.86×10^{-2})	
Larynx	302.15	75% (1.86×10^{-2})	
Trachea	303.15	75% (1.98×10^{-2})	
G0–G2	305.15	83% (2.46×10^{-2})	
G3–G4	310.15	99.5% (3.92×10^{-2})	
Outlets	310.15	99.5% (3.92×10^{-2})	Pressure outlet

[1] Please refer to Eq. (14) for the velocity profile of the breathing cycle before vaccine injection. The inlet velocity becomes zero at the end of exhalation phase when vaccine injection begins.

Table 2 Droplet compositions and properties

Component	Component mass fraction			
	GG to λ-C mass ratio = 75:25		GG to λ-C mass ratio = 50:50	GG to λ-C mass ratio = 25:75
	Case 1 0.2%[1]	Case 2 1%	Case 3 1%	Case 4 1%
PBS	4.70×10^{-2}	4.66×10^{-2}	4.66×10^{-2}	4.66×10^{-2}
GG	1.43×10^{-3}	7.08×10^{-3}	4.72×10^{-3}	2.36×10^{-3}
λ-C	4.75×10^{-4}	2.36×10^{-3}	4.72×10^{-3}	7.08×10^{-3}
Water	9.51×10^{-1}	9.44×10^{-1}	9.44×10^{-1}	9.44×10^{-1}

T (K)	M_W (g/mol)				Density (g/cm^3)			
	PBS	GG	λ-C	Water	PBS	GG[2]	λ-C[3]	Water
298.15	65.22	128.61	579.5	18.01	2.09	0.5	0.034	1.00

[1] Total polymer concentration (%w/v)

[2] Morrison et al., 2016.

[3] Density of vaccine solution was reported 1010 kg/m^3 by Moakes et al. (2021). Density of λ-C was calculated accordingly.

in Table A3 in the Appendix. There are approximately $4×10^8$ epithelial cells in the upper respiratory tract of humans (Baccam et al., 2006). It was also estimated that 1%–20% of these cells express ACE-2 receptors (Hou et al., 2020; Sungnak et al., 2020). In this study, it was assumed that 10% of the $4×10^8$ epithelial cells have ACE-2 and are susceptible to being infected by SARS-CoV-2 (Vaidya et al., 2021). Since there was no available clinical data for young children, the initial number of susceptible epithelial cells with ACE-2 to SARS-CoV-2 infection, $E_0 = 4×10^7$, which was reported for adults, was employed for the 6-year-old child. Based on the

clinical samples, the viral titer was $VT_0 = 2×10^5$ copies/mL on day 0 after symptoms onset (Pan et al., 2020). Therefore, $VT_0 = 2×10^5$ copies/mL was also used for the HCD simulations in this study. Initial value counts for immature dendritic cells, naive CD4+ T cells, and naive B cells were considered 1000 cells (Lee et al., 2009). The initial counts of uninfected macrophages and NK cells residing in the lung compartment are assumed to be 1000 cells as well. The initial values of other cell counts were set to zeros. After HCD model calibration, E_0 was updated based on the vaccine coverage of ACE-2 in OR obtained by CFPD analysis.

4 Numerical simulation

4.1 Geometry and mesh

The respiratory system model employed for the current study is shown in Fig. 1(a). The model comprises the entire upper airways (nasal cavity, oral cavity, pharynx, larynx, and trachea) and the first five generations (G) (i.e., G0–G4) of the tracheobronchial (TB) tree. Specifically, the larynx-to-trachea region was reconstructed based on the CT scan images of a 6-year-old female. The mouth, nose, nasopharynx, and pharynx were adopted from a subject-specific upper airway geometry reconstructed based on the magnetic resonance imaging (MRI) data of a 47-year-old healthy male. The geometry was scaled down in size to be compatible with the anatomical geometry dimensions for the 6-year-old age group. The G0–G4 TB tree starting from G0 to G4 was generated with anatomical features using a stochastic algorithm (Kitaoka, 2011). The surface areas of different regions of the geometry are listed Table 3.

Unstructured polyhedron-based meshes were generated for the upper airway geometry using Ansys Fluent Meshing 2020 R1 (Ansys Inc., Canonsburg, PA, USA). Five near-wall prism layers were generated to precisely capture boundary layer flow regimes and laminar-to-turbulence transition sites. Details of the surface mesh are shown in Fig. 1(b) as well as the OR (in dark gray). To find the final mesh that can provide the optimal balance between computational efficiency and accuracy, three meshes with different element sizes were generated for the mesh independence test. Mesh specifications are listed in Table 4. Polyhedron-based volume cells of the meshes in a cross-section of the nasal cavity are visualized in Figs. 1(c)–1(e).

The normal breathing frequency of a 6-year-old child was considered 25 breaths/min (Fleming et al., 2011), and the tidal volume for a 21 kg child (average weight of children at 6 years old) was considered 7 mL/kg (Koomen et al., 2021). Employing the above-mentioned specifications, the steady-state inlet flow velocity employed at each nostril for the mesh independence test was 4.5 m/s (i.e., the average
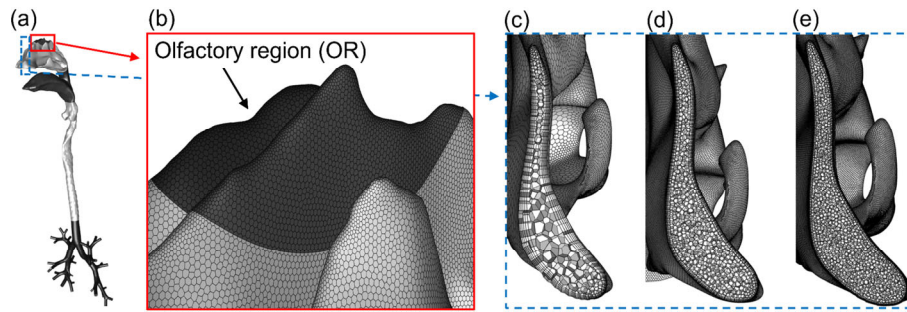
Fig. 1 Respiratory system geometry and mesh: (a) the upper airway geometry from nasal cavity to G4 of a 6-year-old child; (b) the surface mesh of the olfactory region (i.e., the dark gray region). Volume mesh details of (c) Mesh 1 (coarse), (d) Mesh 2 (final mesh), and (e) Mesh 3 (most refined).

Table 3 Surface area of different regions in the respiratory system model

	Respiratory system model	Nasal cavity	Olfactory regions
Surface area (m^2)	13.1×10^{-3}	47.05×10^{-4}	17.8×10^{-5}

Table 4 Specifications of meshes generated for the independence test

Mesh number	Cell counts	Iterations needed for convergence	y^+
Mesh 1	1,150,080	131	98% <1
Mesh 2 (final mesh)	3,725,651	241	99% < 1
Mesh 3	6,550,677	375	100% < 1

inhalation velocity). Using the average inhalation velocity, an idealized sinusoidal breathing waveform was employed for this study. The transient breathing velocity V at the nostrils is defined as a function of time t, i.e.,

$$V = 7.12\sin\left(2\pi \frac{t}{\tau}\right) \tag{14}$$

where $\tau = 2.4$ s is the duration of one breathing cycle.

The convergence criteria were set to 1×10^{-4}. The SIMPLE scheme was employed for pressure–velocity coupling, and the first-order upwind scheme was used for the spatial discretization of pressure, turbulent kinetic energy, and specific dissipation rate. Figures 2(a)–2(c) show the comparisons of the velocity profiles along three lines selected at different locations in the respiratory system. The comparison indicates that Mesh 2 is the most efficient mesh to obtain numerical results with acceptable accuracy.

4.2 CFPD setup

Ansys Fluent 2022 R1 (Ansys Inc., Canonsburg, PA, USA) was utilized for CFPD simulations. The flow field is transient with the flow time step size $\Delta t_f = 2 \times 10^{-3}$ s, which is determined by a time-step independence test. The transient breathing waveform (i.e., Eq. (14)) was applied at the nostrils. As mentioned in Section 3, vaccine droplets were injected into the left nasal cavity after one breathing cycle simulated, with the initial velocity equal to 8.5±3.5 m/s (Xi et al., 2021). Droplet size distribution was considered polydisperse ranging from 20 to 300 μm (Xi et al., 2021), and 40 different size bins (40,000 particles) were set to be injected. The spray nozzle diameter was 0.2 mm (Kapadia et al., 2019), and the insertion depth was 5 mm from the nostril. The spray nozzle was set to make an angle of 35° with the gravitational direction, assuming that the head-to-foot direction is aligned with gravity.

The droplet time step size is 1×10^{-3} s. Constant binary diffusivity (i.e., $D_w = 5.05 \times 10^{-5}$ m²/s) and piecewise-linear saturation vapor pressure were set for the liquid water
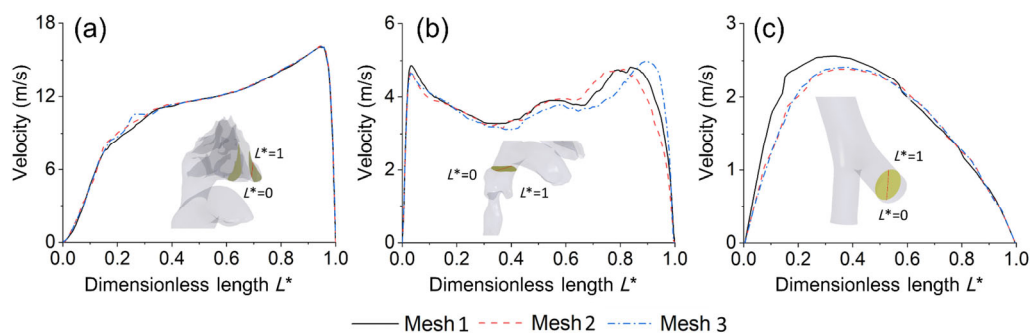

Fig. 2 Airflow velocity profile comparisons using multiple meshes along with selected lines in (a) nasal cavity, (b) larynx, and (c) G4.

component in vaccine droplets. Therefore, the saturation vapor pressure is temperature-dependent and is defined as

$$P_{sat}(T) = P_{sat,n} + \frac{P_{sat,n+1} - P_{sat,n}}{T_{n+1} - T_n}(T - T_n),\ 1 \le n \le N \quad (15)$$

where N is the number of segments between maximum and minimum temperature. Saturation vapor pressure data used in Eq. (15) were obtained from an engineering handbook (Perry et al., 1984).

Furthermore, in-house user-defined functions (UDFs) were revised and compiled in the computational cases for

(a) transient inhalation and exhalation profile;

(b) droplet Brownian motion induced force;

(c) recovering anisotropic near-wall turbulence fluctuation velocities and drag coefficient;

(d) calculating multi-component droplet size change;

(e) updating droplet density;

(f) storing locations and physical properties of droplets deposited; and

(g) storing the area of the surfaces the droplets landed on.

Numerical simulations were performed on a local Dell Precision T7810 workstation (Intel® Xeon® Processor E5-2643 v4 with dual processors, 64 cores, and 128 GB RAM) and a local Dell Precision T7910 workstation (Intel® Xeon® Processor E5-2683 v4 with dual processors, 64 cores, and 256 GB RAM). Using 32 cores, the CPU time for the simulation of one breathing cycle to initialize the case was approximately 75 h, and the nasal spray droplet transport simulations took approximately 0.05 h.

4.3 HCD setup

To solve the system of stiff nonlinear coupled ODEs that can quantitatively describe immune response dynamics, an in-house MATLAB code was developed. An ODE solver (i.e., ode23t) capable of using adaptive time step size for resolving nonlinear stiff ODEs was employed. The initial values of the variables are provided in Table A3 in the Appendix. Temporal behavior and dynamics of the viral titer and innate immunity were modeled in the lung compartment. Dendritic cell maturation, naive T cell activation, and antibodies and effector cell proliferation are simulated in the lymphatic compartment. Two and a half (i.e., 2.5) days after the onset of the symptoms, the antigen-specific antibodies are detectable in the lung compartment (Long et al., 2020). Therefore, a delay time, $\tau_D = 1$ d, was considered to take into account the time needed for adaptive immune response for SARS-CoV-2 to start being activated, and another delay time, $\tau_T = 2$ d, was included in the optimization to observe the adaptive immunity

dynamics in the lung compartment. The simulation was performed for 30 d in the lung compartment and 28 d (from day 1 to day 29) in the lymphatic compartment. The HCD model coefficients were well-calibrated by minimizing the root mean squared error (RMSE) between available clinical data and HCD modeling results.

$$RMSE = \sqrt{\frac{1}{N}\sum(\log_{10}\varPhi_{exp} - \log_{10}\varPhi_{HCD})^2} \quad (16)$$

where $\varPhi_{exp}$ and $\varPhi_{HCD}$ are the experimental and computational data, respectively.

The details of the HCD model calibrations are discussed in Section 5.2. After calibration, the initial epithelial cell counts E_0 obtained from CFPD simulation results were introduced to the HCD model for immune response analysis after intranasal vaccine injection (please see Section 3 for more details).

5 Model validation and calibration

5.1 CFPD model validation

To validate the CFPD model, pure water droplet evaporation was simulated and compared with experimental data. Specifically, a 16 μm pure water droplet was released into a square duct. The geometric dimensions of the duct are 0.15 m in height, 0.15 m in width, and 5.5 m in length. Ambient RH and temperature were 70% and 296.15 K constant in the duct, respectively. Inlet air velocity was 1 m/s. Droplet initial temperature was set to 296.15 K, and its initial velocity was 0 m/s. Figure 3 compares the simulation results and experimental data reported by El et al. (1974) on the droplet radius change. Good agreement can be observed between numerical simulation and experimental measurements, indicating that the CFPD model employed in this study can accurately predict the water evaporation/condensation rate in the vaccine droplets simulations.
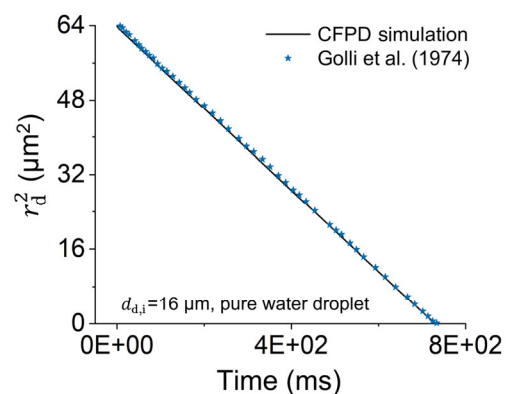

Fig. 3 CFPD model validation for pure water droplet evaporation.

5.2   HCD model calibration

Calibrated with clinical data obtained from human patients who were tested positive for SARS-CoV-2, the code estimated the optimized values for the viral load and the immune response coefficients. For optimizing the coefficients, the "multi-objective optimization using genetic algorithm" (i.e., gamultiobj in MATLAB) was employed. Specifically, a set of coefficient values were computed using the above-mentioned optimization algorithm by minimizing the RMSE magnitude between the experimental datasets obtained from COVID-19 patients (Long et al., 2020; Pan et al., 2020) and the corresponding data predicted by the HCD model (see Eq. (16)). Through the optimization, some coefficient values were considered fixed (see the Appendix for more details). The coefficient values optimized are listed in Table A4 in the Appendix.

Comparisons of clinical data and the HCD simulation results after calibration are shown in Fig. 4. Specifically, the fitted curves for viral load and adaptive immune responses for a baseline simulation were compared. RMSE values for cell count curves predicted by the HCD model are reported as well. It can be observed that the HCD model predictions are in good agreement with clinical data on viral clearance and antigen-specific antibody titer time profile. Viral load peaks approximately two to three days after symptoms onset (Fig. 4(a)), which suggests virus production rate per infected epithelial cell is π_V = 2.61 copies/(mL·d). Furthermore, the death rate constant for infected cells is δ_{E_I} = 5 d^{-1}. Viral load starts decreasing at a high rate after peak day mainly because the number of healthy epithelial cells drops, and infectious viruses do not have an environment to replicate themselves in, i.e., virus non-specific clearance. It is shown in Figs. 4(b) and 4(c) that SARS-CoV-2 specific antibodies (IgM and IgG) are not detectable in the lung compartment before day 2 after symptoms onset. After two days, however, the antibodies IgM and IgG travel to the lung from the lymph node to neutralize the viruses at the rate of c_{A_S} = 0.53 (µg·d)$^{-1}$ and c_{A_L} = 1.1 (µg·d)$^{-1}$. Both IgM and IgG levels plateaued after day 15.

6   Results and discussion

6.1   RH distribution in the nasal cavity

Figure 5 shows the water vapor distribution in the nasal cavity at the end of the exhalation phase when the airflow velocity is zero and vaccine spraying begins. Local values of minimum and maximum water vapor mass fraction are reported under and above each cross-section. Besides the closest cross-section to the nostril, the difference between the maximum and minimum water vapor mass fraction at each cross-section is small, indicating the effectiveness of humidification of the nasal passage to the inhaled dry air.

6.2   Influence of multiple parameters on vaccine delivery efficiency to the olfactory region

To find the key parameters that can influence the delivery efficiency of vaccine droplets to the OR, numerical simulations were performed with various initial spray droplet velocities ($V_{d,i}$), spray cone angles (θ), and initial droplet compositions. Figure 6 demonstrates the delivery efficiency of vaccine droplets to OR, influenced by the above-mentioned parameters.

Specifically, Fig. 6(a) shows the deposition fraction (DF) of droplets versus spray cone angle θ for four different droplet initial velocities. It can be observed that with the same $V_{d,i}$, droplet DF in OR decreases with the increase in θ. For example, with $V_{d,i}$ = 5 m/s, DF for θ = 5° is approximately 5%, while DF decreases lower than 1.5% for θ = 15°. Therefore, Fig. 6(a) indicates that a smaller spray angle is recommended for higher vaccine delivery efficiency to the OR for the 6-year-old child. The reason for this trend is that with a wider spray cone angle, more micro-sized droplets can intercept the airway wall due to the complex morphology and narrow nasal airway passage. Furthermore, Fig. 6(a) also shows that varying $V_{d,i}$ has a negligible impact on the vaccine droplet DF in OR, which is because the initial droplet velocity ($V_{d,i}$ = 5–12 m/s) and momentum are relatively high, the viscous dissipation effect induced by the drag force is insignificant. In addition, due to the small
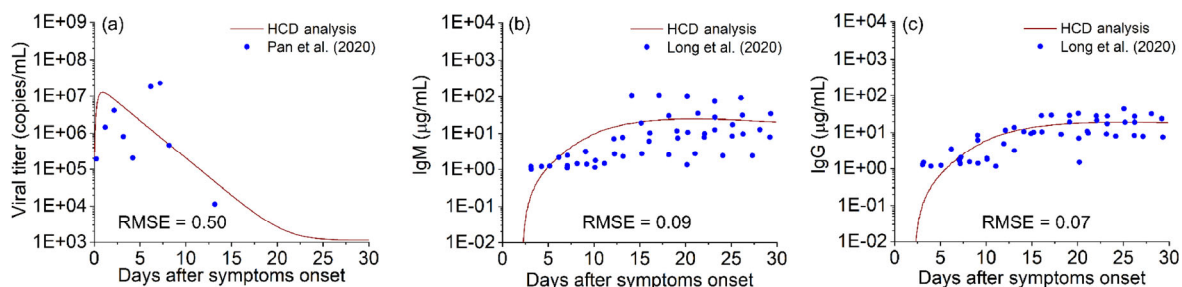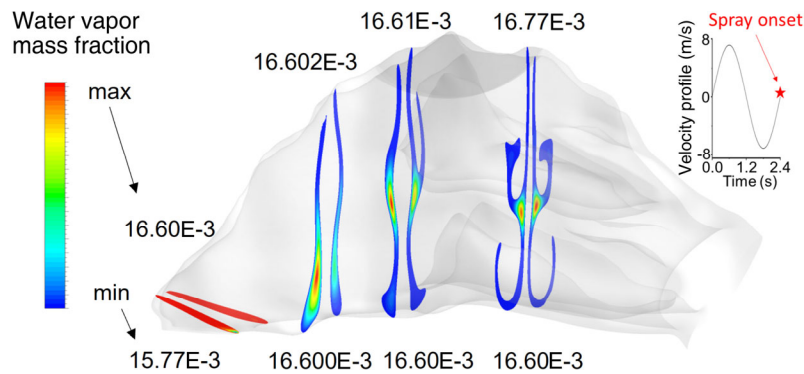

Fig. 4   Comparisons of optimized HCD modeling results and available clinical data to predict SARS-CoV-2 infection induced temporal variations in (a) viral titer, (b) short-lived antibodies (IgM), and (c) long-lived antibodies (IgG).

Fig. 5 Mass fraction distribution of water vapor in multiple cross-sections of the nasal cavity at the end of exhalation when vaccine droplets were injected.
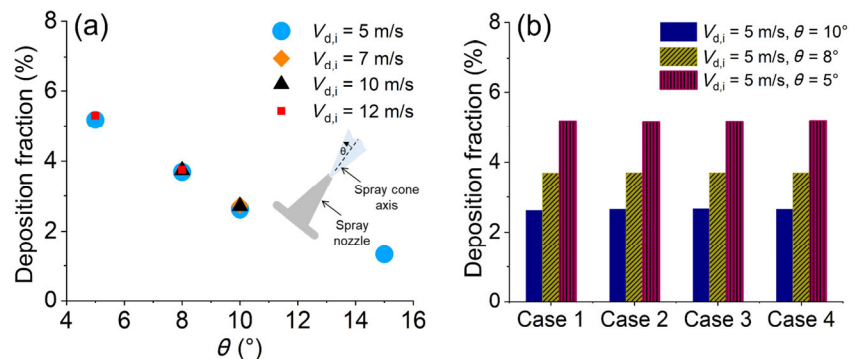

Fig. 6 Deposition fractions (DF) of the nasal spray vaccine droplets in the olfactory region (OR) with (a) different droplet injection velocities and spray cone angles; (b) different spray cone angles and droplet initial compositions.

droplet diameter, the gravitational sedimentation effect on droplet trajectory is negligible compared to the high initial momentum of the droplets. Therefore, although the droplet residence time was influenced by $V_{d,i}$, the droplet trajectories and deposition locations are highly similar for the droplets released at the same position with the same θ and different $V_{d,i}$.

Figure 6(b) shows regional DFs of vaccine droplets in OR with different droplet initial compositions (see Table 3 for the initial droplet composition associated with each case) and injection cone angles θ (5°, 8°, and 10°). Since $V_{d,i}$ has negligible influence on droplet DF in OR, $V_{d,i}$ was kept constant at 5 m/s in Fig. 6(b). Figure 6(b) demonstrates again that a wider cone angle leads to lower vaccine delivery efficiency to OR. In contrast, droplet composition does not significantly influence the DF of vaccine droplets to the targeted site (i.e., OR). For all four compositions, water liquid mass fraction is approximately 95% in the droplet, while other non-evaporable components constitute only 5% in mass. Although the densities of the non-evaporable components are different, the variation in their mass fraction among Cases 1–4 (see Table 2) is small. Hence, there will not be a considerable change in droplet transport and deposition associated with various compositions.

To unveil more underlying droplet transport dynamics

that can be impacted by $V_{d,i}$ and θ, Figs. 7(a)–7(f) show the droplet residence time and droplet diameter change ratio ($d_{d,f} / d_{d,i}$) as a function of initial droplet diameter $d_{d,i}$, spray cone angle θ, as well as the initial droplet composition. Specifically, Figs. 7(a)–7(c) show the droplet residence time with different initial droplet compositions (see Table 2 for details). It can be observed that the initial droplet composition has a negligible effect on droplet residence time, which is also due to the fact that the changes in the initial droplet composition do not significantly influence the initial droplet mass and evaporation/condensation characteristics. It can also be seen that droplet residence time is very short, indicating the quick deposition after injection as well as the short time for water evaporation or condensation. For example, vaccine droplets with $V_{d,i} = 5$ m/s need less than 0.03 s to reach OR. Accordingly, as shown in Figs. 7(d)–7(f), droplet size change was not significantly influenced by the initial droplet composition, $V_{d,i}$, or θ. The evaporation can be considered the same for all cases, which is, as mentioned above, because they all consist of 95% evaporable water and 5% non-evaporable components in mass. Therefore, water thermodynamic behavior is what determines droplet size change, which is the same for all cases. Droplet diameter change ratio $d_{d,f} / d_{d,i}$ for different initial droplet compositions and θ are all higher than 99.5%. This is because of
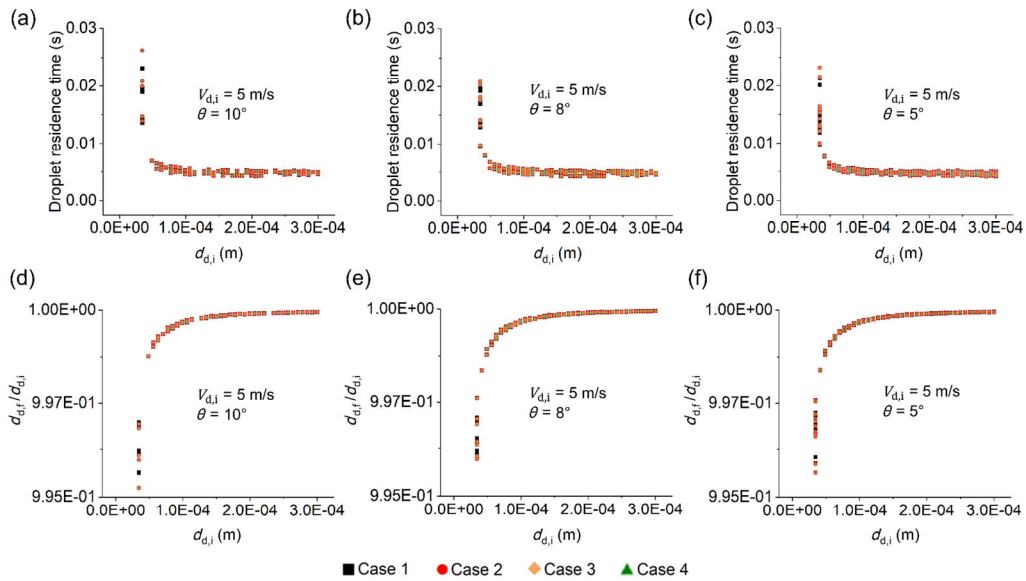
Fig. 7 Vaccine droplet residence time and size change ratio as functions of $d_{d,i}$, θ, and the initial droplet composition: (a)–(c) droplet residence time; and (d)–(f) droplet size change ($d_{d,f} / d_{d,i}$) versus droplet initial size $d_{d,i}$ for different spray cone angle θ with initial velocity $V_{d,i}$ of 5 m/s.

the short droplet residence time, which limited the total mass of water evaporation/condensation. In contrast, the droplet size change is noticeably influenced by the initial droplet diameter $d_{d,i}$. Smaller $d_{d,i}$ induced higher water evaporation/condensation and droplet shrinkage, which is due to the Kelvin effect. Specifically, a smaller initial droplet diameter means higher surface curvature, leading to a faster evaporation/condensation rate.

Figures 8(a)–8(c) plot the local distribution of vaccine droplets after they were sprayed into the nasal cavity. The effects of droplet compositions and cone angles on vaccine delivery to OR can be observed. It has been demonstrated that vaccine composition does not affect droplet distribution in OR/nasal cavity. The spray cone angle θ slightly affects droplet distribution. A wider cone angle ($\theta = 10°$) leads to a relatively better VC of OR by droplets than a smaller cone angle ($\theta = 5°$). Nonetheless, as it was discussed earlier, the simulation outcomes suggest that a larger cone angle θ can lead more droplets to be trapped in unexpected regions

other than the OR for SARS-CoV-2 vaccines. Assessment of VC and its influence on immune response and COVID-19 severity is a crucial step that needs to be taken into account to design an efficient intranasal vaccine spray.

6.3 Influence of nasal spray vaccine on viral replications predicted by the CFPD–HCD model

Figure 9 demonstrates the VC obtained from CFPD simulations and its influence on infection progression predicted by HCD analysis. In Fig. 9(a), vaccine droplets (injected with different cone angle θ) deposited in OR are visualized. With $\theta = 15°$, DF = 1% of the droplets (see blue droplets in Fig. 9(a)) can deposit in OR, which covers 1.8% of the OR surface area. Although the droplet deposition with $\theta = 15°$ is more scattered on the OR surface, the epithelial cells that can be covered by those droplets are not higher than the rest due to the fact that fewer droplets are deposited. By reducing θ from 15° to 5°, higher DF (i.e., 5%)
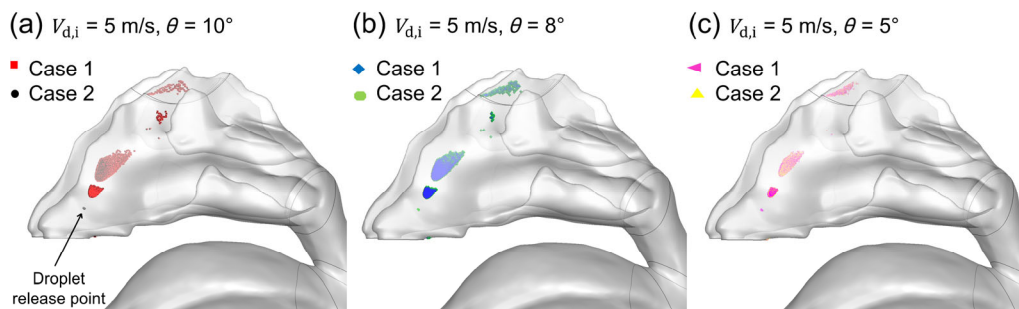

Fig. 8 Local deposition of vaccine droplets in the nasal cavity for two initial droplet compositions (Case 1 and Case 2) at $V_{d,i}$ = 5 m/s with the spray cone angle being (a) $\theta = 10°$, (b) $\theta = 8°$, and (c) $\theta = 5°$.
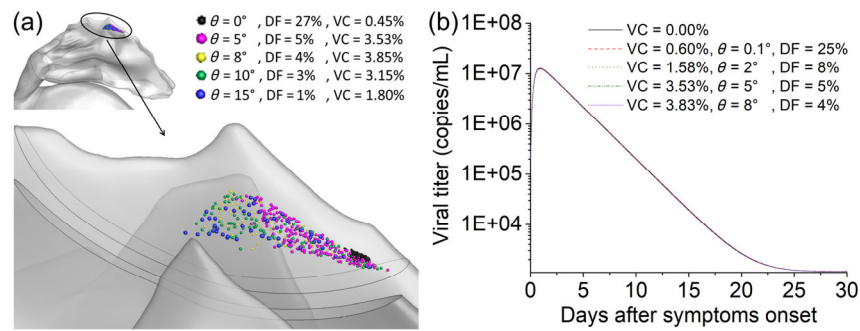
Fig. 9 VC and its influence on viral titer kinetics predicted by the CFPD–HCD model: (a) visualization of VC areas with different spray cone angles θ; (b) viral titer kinetics with different VCs obtained from CFPD simulation results.

and VC (i.e., 4%) can be achieved. Nonetheless, reducing the cone angle further (i.e., $0° < \theta < 5°$) resulted in a decrease in VC despite the increased DF (see Fig. 9(a)). Therefore, to seek the highest VC, $\theta = 8°$ is recommended. In Fig. 9(b), the impact of VC on viral titer kinetics is plotted. It can be observed that even with the highest VC, which is approximately 4% for $\theta = 8°$, it is not able to trigger a sufficiently strong effect on varying the viral peak and its decaying trend. It is because that using the conventional atomization technique and available nasal spray nozzle openings, the vaccine droplets still cannot cover a sufficiently large area of OR (ACE-2-rich site). Therefore, the number of susceptible epithelial cells that can be infected by the virus for reproduction was not significantly reduced. However, if the vaccine droplet size distributions and release nozzle can be modified, it is possible that the VC can be further increased. Based on the comparisons shown in Fig. 9(b), it can be hypothesized that further increasing VC can lead to a noticeable reduction in the viral titer peak, which has been proven by the comparisons shown in Fig. 10.

6.4 HCD analysis of viral titer kinetics

To test the hypothesis mentioned at the end of Section 6.3, the effects of VC (the percentage of epithelial cells covered by the vaccine droplet deposition) and initial viral titer of SARS-CoV-2 on temporal dynamics of viral titer and its peak are predicted and compared in Fig. 10(a). VC percentages were artificially varied from 0 to 99%. Specifically, VC = 0 represents the infection case without intranasal vaccine administration. It is shown that the increase in VC, which indicates fewer susceptible epithelial cells to be infected by SARS-CoV-2 invasion, can reduce the viral titer peak value. Indeed, the peak value of viral titer is reduced from 1×10^7 to 3×10^6 approximately if the vaccine droplets can cover up to 70% of the OR surface. It can also be found in Fig. 10(a) that the viral agents will hardly duplicate themselves if VC can reach 99%. To further study the influence of the initial value of viral titer VT_0 on the viral titer peak, VT_0 was reduced, and the results are shown in Fig. 10(b) with VC = 0. It can be observed that changing from 1×10^3 copies/mL to 2×10^5 copies/mL, VT_0 has negligible influence on the viral titer time profile if the numbers of susceptible epithelial cells are similar. Therefore, Figs. 10(a) and 10(b) demonstrate that the effectiveness of the intranasal COVID-19 vaccine is highly dependent on the percentage of epithelial cells that can be covered by the aerosolized vaccine droplets. The nasal spray formulation and administration strategy must be optimized to maximize the VC, thereby reducing the possibility for SARS-CoV-2 reproduction.

7 Conclusions

Using an experimentally calibrated and validated CFPD–HCD model, this study predicted the transport of intranasal
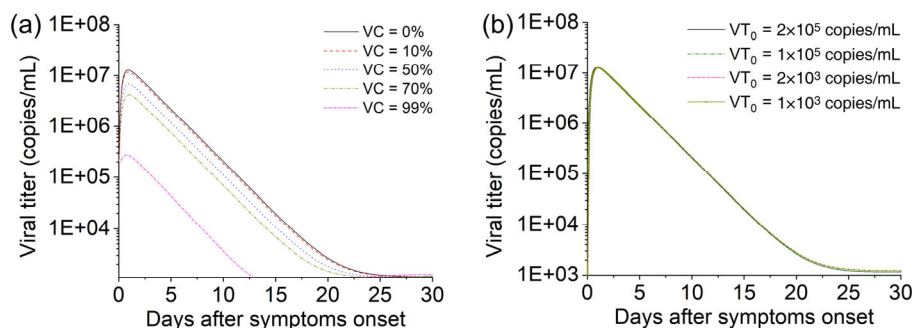

Fig. 10 Effects of (a) vaccine coverage and (b) initial viral titer on time profiles of SARS-CoV-2 viral titer.

SARS-CoV-2 vaccine droplets delivery to ACE-2-rich regions (i.e., the olfactory region) in the nasal cavity of a 6-year-old female, as well as the vaccine influence on boosting local (mucosal) immunity against COVID-19 infection. Key conclusions are summarized below.

(1) Vaccine droplet size change dynamics and deposition fractions in the olfactory region were not significantly influenced by initial droplet velocity or initial droplet composition.

(2) Spray cone angle has a significant influence on vaccine droplet deposition fraction in the olfactory region, but has a negligible impact on droplet residence time and size change. To pursue the highest deposition fraction in the olfactory region, the most efficient cone angle is $\theta = 5°$. In contrast, to cover the most epithelial cells in the olfactory region, the most efficient cone angle is $\theta = 8°$.

(3) Using the administration strategies investigated in this study, vaccine droplets can only occupy approximately 4% of the epithelial cells in the olfactory region, which is not sufficient for boosting immunity against SARS-CoV-2. To trigger effective immunity using intranasal COVID-19 vaccine spray, it is necessary to optimize the vaccine formulation and physical properties to enable the nasal spray to cover 99% of the epithelial cells in the olfactory region.

8 Limitations of the current study and future work

For this study, we encountered some limitations, and some simplifications needed to be made. The simplifications were:

(1) Instead of a realistic breathing profile, an idealized sinusoidal waveform was employed for the CFPD simulation.

(2) No mucus lining was included in the nasal cavity.

(3) The subject was not systemically (intramuscularly) vaccinated.

(4) The upper respiratory tract model was scaled down and connected to the larynx/trachea model of the 6-year-old child. Each vaccine droplet could cover the entire face cell it landed on. The lack of available clinical data for young children with COVID-19 caused us to use the adult clinical data that were reported in the literature.

In the future, to obtain more realistic flow field dynamics in the respiratory system, a realistic subject-specific breathing profile is recommended to be employed. Smaller spray droplets can be studied as well to see if they can improve vaccine delivery efficiency. Furthermore, it has been observed that mucus clearance and spray-liquid motion will alter the resting area of the spray droplets deposited on the mucus lining. Rygg et al. (2016) showed that mucus clearance will transport the drugs that deposit on the mucus lining in the nasal cavity, which may or may not be in favor of drug delivery to targeted sites. Some of the drugs can be transported to the targeted site, while some might be completely removed from the nasal cavity. Kolanjiyil et al. (2022) reported that deposited spray liquid moved in the gravitational direction as well as inhalation flow direction using CFPD and Eulerian film model. Therefore, to provide more realistic resting site and VC of the COVID-19 vaccine droplets, post-deposition liquid film motion in the nasal cavity can be simulated by employing the Eulerian film model as a future work. Additionally, the entire upper respiratory system geometry of children could be constructed using CT/MRI images instead. To predict the local (mucosal) immune response triggered by nasal vaccines against COVID-19 more accurately using the HCD model, age-specific clinical data from young patients diagnosed with SARS-CoV-2 is recommended for model calibration. Finally, the immunity triggered by SARS-CoV-2 intramuscular vaccines can be involved along with intranasal vaccines in HCD modeling to predict the robustness of topical and systemic immunization.

Appendix

In Table A1, governing equations of the HCD model for non-specific immunity are provided. Viruses that bind to the susceptible and permissive target epithelial cells, E, infect them at a rate of $\beta_E VE$. The infected cells are in the latent phase, E_{IL}, at first and will become detectable, E_I, at the rate of $\delta_{E_{IL}} E_{IL}$. The infected cells die at the rate of $\delta_{E_I} E_I$. Viruses use the machinery of the infected cells and replicate themselves at the rate of $\pi_V E_I$. Infectious virions that are released into the extracellular area of the lung tissue activate resting macrophages, M_R, whose defensive mechanism is to phagocyte and dispose of dead cells and cell debris as well as invading influenza viruses at the rate of $\alpha V M_R / (V_{50} + V)$. The death rate of tissue resting and activated macrophages are $\delta_{M_R} M_R$ and $\delta_{M_A} M_A$, respectively. It has been reported that macrophages can become infected, M_I, with the rate of $\lambda M_A V$ and replicate the viruses at the rate of $\pi_{M_I} M_I$ (Pawelek et al., 2016). Infected macrophages die at the rate of $\delta_{M_I} M_I$.

Pre-death innate defensive response of the infected cells results in the production of interferons, F, by the rate of $\pi_F E_I$. Interferons send signals to the neighboring cells to be prepared to resist, E_R, to a viral infection with Φ_{EF} in rate. The cells refracted to the infection will become susceptible to infection again at the rate of $\delta_{E_R} E_R$. As well as signaling the neighboring uninfected cells, interferons activate resident natural killer, K, cells at the rate of $\phi_k FK$, which are lymphocytes of innate immunity, to secret cytokines and kill the detectable and latent-phased infected cells by inducing

them to undergo apoptosis (Parham, 1950) at the rate of $\kappa_k E_I K$ and $\kappa_k E_{IL} K$, respectively. Resident and activated natural killer cells die respectively at the rate of $\delta_k K$ and $\delta_k K_A$. Resident dendritic cells, D, who act as sentinels that take up pathogens and their products and become virus loaded, D_I, by the rate of $\beta_D D V$. The infected dendritic cells activate the natural killer cells to become effector cells. If effector natural killer cells outnumber the infected dendritic cells, they can kill the dendritic cells at the rate of $\delta_{D_I} D_I$. However, if the natural killer cells are scarce and outnumbered by infected dendritic cells, they lead the infected dendritic cells to mature into the form that initiates adaptive immunity. Infected dendritic cells act as cellular messengers and migrate to the lymph node to call up adaptive immune responses (Parham, 1950).

On encountering the antigen recognized by their antigen receptors in the lymphatic compartment, naive CD4$^+$ T cells and CD8$^+$ T cells become activated by antigens at the rate of $\pi_H = \pi_{H1} D_M / (\pi_{H2} + D_M)$ and $\pi_T = \pi_{T1} D_M / (\pi_{T2} + D_M)$, respectively. Thereafter, activated CD4$^+$ T and CD8$^+$ T cells differentiate into effector CD4$^+$ T cells (helper T cells) and CD8$^+$ T cells (cytotoxic T cells) at the rate of $\rho_H = \rho_{H1} D_M / (\rho_{H2} + D_M)$ and $\rho_T = \rho_{T1} D_M / (\rho_{T2} + D_M)$, respectively. Through this process, effector CD4$^+$ T cells help the mature dendritic cells to activate naive CD8$^+$ T cells. The death rate of effector CD4$^+$ T and CD8$^+$ T cells are $\delta_H = \delta_{H1} D_M / (\delta_{H2} + D_M)$ and $\delta_T = \delta_{T1} D_M / (\delta_{T2} + D_M)$, respectively. Thereafter, effector T cells travel to the infection site. Effector CD4$^+$ T cells are cytokines that only help cytotoxins to function. They do not directly eliminate infected cells. Cytotoxic T cells kill the infected cells at the rate of $\kappa_E E_I \gamma T_E (t - \tau_T)$ during the adaptive immunity by inducing apoptosis, similar to natural killer cells during innate immunity. The model equations for adaptive immunity are provided in Table A2. Naive B cells exposed to the antigens become activated at the rate of $\pi_B = \pi_{B1} D_M / (\pi_{B2} + D_M)$ and next, they form a cognate pair with Helper CD4$^+$ T cells to proliferate at the rate of $\rho_{BA} = \rho_{B1}(D_M + h H_E) / (D_M + h H_E + \rho_{B2})$. Activated B cells differentiate into short-lived plasma cells and long-lived memory B cells at the rate of $\pi_s B_A$ and $\pi_L H_E B_A$, respectively. Short-lived plasma cells secret IgM at the rate of $\pi_{A_S} P_S$ whose clearance rate is $\delta_{A_S} A_S$. Long-lived plasma cells secret IgG at the rate of $\pi_{A_L} P_L$. IgG have a clearance rate of $\delta_{A_L} A_L$. These antibodies circulate in the bloodstream and enter the infected site to neutralize viruses. Definition of model variables and their initial values are stated in Table A3.

The estimated values of parameters obtained from HCD model calibration with SARS-CoV-2 clinical data are presented in Table A4. To simplify the calibration, the conversion rate of cells that form latent phase to infected cells $\delta_{E_{IL}} = 3$ d^{-1}, death rate of infected epithelial cells $\delta_{E_I} = 5$ d^{-1}, death rate of uninfected macrophages $\delta_{M_R} = 0.06$ d^{-1}, death rate of activated macrophages $\delta_{M_A} = 0.04$ d^{-1}, and the death rate of the infected macrophages $\delta_{M_I} = 0.04$ d^{-1} were kept constant (they are marked by a plus sign beside them in Table A4). The values were chosen based on the data reported in the literature (Pawelek et al., 2016; Vaidya et al., 2021).

Table A1 ODEs of immune response in lung compartment

$\dfrac{d}{dt} E = -\beta_E V E - \Phi F E + \delta_{E_R} E_R$	(A1)
$\dfrac{d}{dt} E_{IL} = \beta_E V E - \delta_{E_{IL}} E_{IL} - \kappa_k E_{IL} K$	(A2)
$\dfrac{d}{dt} E_I = \delta_{E_{IL}} E_{IL} - \delta_{E_I} E_I - \kappa_E E_I \gamma T_E(t - \tau_T) - \kappa_k E_I K$	(A3)
$\dfrac{d}{dt} V = (1 - \varepsilon_1)(\pi_V E_I + \pi_{M_I} M_I) - c_V V - c_M M_A V$ $\qquad - c_{A_S} A_S - c_{A_L} A_L$	(A4)
$\dfrac{d}{dt} M_R = \delta_{M_R}(M_{R0} - M_R) - \dfrac{(1 - \varepsilon_2)\alpha V M_R}{V_{50} + V}$	(A5)
$\dfrac{d}{dt} M_A = \dfrac{(1 - \varepsilon_2)\alpha V M_R}{V_{50} + V} - \lambda M_A V - \delta_{M_A} M_A$	(A6)
$\dfrac{d}{dt} M_I = \lambda M_A V - \delta_{M_I} M_I$	(A7)
$\dfrac{d}{dt} F = \pi_F E_I - \delta_F F$	(A8)
$\dfrac{d}{dt} K = \delta_k(K_0 - K) - \phi_k F K$	(A9)
$\dfrac{d}{dt} K_A = \phi_k F K - \delta_k K_A$	(A10)
$\dfrac{d}{dt} E_R = \phi F E - \delta_{E_R} E_R$	(A11)
$\dfrac{d}{dt} D = \delta_D(D_0 - D) - \beta_D D V$	(A12)
$\dfrac{d}{dt} D_I = \beta_D D V - \delta_{D_I} D_I$	(A13)

Table A2 ODEs of immune response in lymphatic compartment

$\dfrac{d}{dt} D_M = k_D D_I(t - \tau_D) - \delta_{D_M} D_M$	(A14)
$\dfrac{d}{dt} H_N = \delta_{H_N} H_{N0} - \delta_{H_N} H_N - \pi_H(D_M) H_N$	(A15)
$\dfrac{d}{dt} H_E = \pi_H(D_M) H_N + \rho_H(D_M) H_E - \delta_H(D_M) H_E$	(A16)
$\dfrac{d}{dt} T_N = \delta_{T_N}(T_{N0} - T_N) - \pi_T(D_M) T_N$	(A17)
$\dfrac{d}{dt} T_E = \pi_T(D_M) T_N + \rho_T(D_M) T_E - \delta_T(D_M) T_E$	(A18)
$\dfrac{d}{dt} B_N = \delta_B B_{N0} - \delta_B B_N - \pi_B(D_M) B_N$	(A19)

(Continued)

$$\frac{d}{dt}B_A = \pi_B(D_M)B_N + \rho_{B_A}(D_M + hH_E)B_A$$
$$- \delta_{B_A}B_A - \pi_s B_A - \pi_L H_E B_A \qquad (A20)$$

$$\frac{d}{dt}P_S = \pi_s B_A - \delta_S P_S \qquad (A21)$$

$$\frac{d}{dt}P_L = \pi_L H_E B_A - \delta_L P_L \qquad (A22)$$

$$\frac{d}{dt}A_S = \pi_{A_S}P_S - \delta_{A_S}A_S \qquad (A23)$$

$$\frac{d}{dt}A_L = \pi_{A_L}P_L - \delta_{A_L}A_L \qquad (A24)$$

Table A3   Definition of HCD variables and their initial values

Variable	Definition	Initial value
E	Uninfected epithelial cells	4×10^7
E_{IL}	Epithelial cells in eclipse phase	0
E_I	Infected epithelial cells	0
V	Viral load (titer)	2×10^5
M_R	Uninfected resting macrophages circulating within the host	1×10^3
M_A	Activated macrophages at the site of the infection	0
M_I	Productively infected macrophages	0
F	Interferons	0
K	Resident NK cells	1×10^3
K_A	Activated NK cells	0
E_R	Uninfected cells that are refractory to infection	0
D	Immature dendritic cells	1×10^3
D_I	Virus-loaded dendritic cells	0
D_M	Mature dendritic cells	0
H_N	Naive CD4 T cells	1×10^3
H_E	Helper T cell	0
T_N	Naive CD8 T cells	1×10^3
T_E	Effector CD8 T cells	0
B_N	Naive B cells	1×10^3
B_A	Activated B cells	0
P_S	Short-lived antibody-secreting plasma cells	0
P_L	Long-lived antibody-secreting cells	0
A_S	Short-lived antibody	0
A_L	Long-lived antibody	0

Table A4   Definitions and values of coefficients in the HCD model

Parameter	Definition	Value (bounds)
β_E	Infection rate of uninfected epithelial cells $(d^{-1}\cdot(copies/mL)^{-1})$	$(1\times10^{-8}, 5.5\times10^{-4})$ 3×10^{-4}
Φ	Interferon-induced antiviral efficacy ((IFN fold change) d^{-1})	$(1\times10^{-8}, 1\times10^{-4})$ 1.1×10^{-5}
δ_{E_R}	Reversion rate from refractory (d^{-1})	$(2, 5)$ 2.97

(Continued)

Parameter	Definition	Value (bounds)
$\delta_{E_{IL}}$	Conversion rate of cells form latent phase to infected (d^{-1})	3^+
κ_k	Killing rate of infected cells by NK cells (d^{-1})	$(1\times10^{-4}, 1\times10^{-2})$ 5.2×10^{-3}
δ_{E_I}	Death rate of infected epithelial cells (d^{-1})	5^+
κ_E	Killing rate of infected cells by cytotoxic (CD8$^+$) T effectors (d^{-1})	$(1\times10^{-5}, 1\times10^{-3})$ 8.4×10^{-4}
ε_1	Drug efficacy	0
π_V	Virus production rate per infected epithelial cells $((copies/mL)\ d^{-1})$	$(2, 6)$ 2.61
π_{M_I}	Virus production rate per infected macrophages $((copies/mL)\ d^{-1})$	$(0.01, 0.08)$ 0.07
c_V	Virus nonspecific clearance rate (d^{-1})	$(0.1, 5)$ 0.5
c_M	Virus clearance rate through death of infected macrophages (d^{-1})	$(1\times10^{-4}, 1\times10^{-2})$ 4.3×10^{-3}
c_{A_S}	Rate of virus neutralization by short-lived antibodies $(d^{-1}\cdot\mu g^{-1})$	$(0.05, 2)$ 5.3×10^{-1}
c_{A_L}	Rate of virus neutralization by long-lived antibodies $(d^{-1}\cdot\mu g^{-1})$	$(0.05, 2)$ 1.1
δ_{M_R}	Death rate of uninfected macrophages (d^{-1})	0.06^*
ε_2	Effect of an anti-inflammatory drug efficacy	0
α	Activation rate of macrophages (d^{-1})	$(0.01, 0.02)$ 1.8×10^{-2}
V_{50}	Viral load for half-maximal activation of macrophages	$(2\times10^{-4}, 3\times10^{-4})$ 2.9×10^{-4}
λ	Infection rate of the activated macrophages	$(1\times10^{-4}, 1\times10^{-2})$ 4.4×10^{-4}
δ_{M_A}	Death rate of activated macrophages (d^{-1})	0.04^*
δ_{M_I}	Death rate of the infected macrophages (d^{-1})	0.04^*
π_F	Secretion rate of interferons by infected cells ((IFN fold change) $d^{-1}\cdot cell^{-1}$)	$(1\times10^{-5}, 1\times10^{-3})$ 0.9×10^{-3}
δ_F	Decay rate of interferons (d^{-1})	$(3, 7)$ 5
δ_k	Death rate of NK cells (d^{-1})	$(2\times10^{-5}, 4\times10^{-5})$ 3.5×10^{-5}
ϕ_k	Activation rate of NK cells by interferons	$(1\times10^{-5}, 1\times10^{-3})$ 0.4×10^{-3}
δ_D	Death rate of immature dendritic cells (d^{-1})	$(9\times10^{-4}, 1\times10^{-3})$ 0.97×10^{-3}
β_D	Infection rate of dendritic cells by unit Corona virus $(d^{-1}\cdot(EID_{50}/mL)^{-1})$	$(1\times10^{-3}, 3\times10^{-3})$ 2.3×10^{-3}
δ_{D_I}	Death rate of infected DCs (d^{-1})	$(5.5, 6.5)$ 6.2
k_D	Antigen processing rate (d^{-1})	$(2, 4)$ 2.5
δ_{H_N}	Death rate of naive CD8$^+$ T cells (d^{-1})	$(7\times10^{-6}, 8\times10^{-6})$ 7.9×10^{-6}
π_{H1}	Maximum activation rate of naive CD4$^+$ T cells (d^{-1})	$(1.2, 1.4)$ 1.26
π_{H2}	Number of D_M cells for half-maximal activation of effector CD4$^+$ T cells	$(120, 140)$ 133

		(Continued)
Parameter	Definition	Value (bounds)
ρ_{H1}	Maximum proliferation rate of naive CD4$^+$ T cells (d^{-1})	(0.1–0.2) 0.17
ρ_{H2}	Number of D_M cells for half-maximal proliferation of effector CD4$^+$ T cells	(3×10^3, 4×10^3) 3.15×10^3
δ_{H1}	Maximum clearance rate of effector CD4$^+$ T cells (d^{-1})	(2–2.5) 2.4
δ_{H2}	Number of D_M cells for half-maximal clearance of effector CD4$^+$ T cells	(1.4, 1.5) 1.43
δ_{T_N}	Death rate of naive CD8$^+$ T cells (d^{-1})	(6×10^{-3}, 7×10^{-3}) 6.3×10^{-3}
π_{T1}	Maximum activation rate of CD8$^+$ T cells from naive CD8$^+$ T cells (d^{-1})	(2, 4) 2.3
π_{T2}	Number of D_M cells for half maximal activation of naive CD8$^+$ T cells	(25, 35) 25.2
ρ_{T1}	Maximum proliferation rate of naive CD8$^+$ T cells (d^{-1})	(1.7, 1.9) 1.8
ρ_{T2}	Number of D_M cells for half-maximal proliferation of effector CD8$^+$ T cells	(300, 350) 325
δ_{T1}	Maximum clearance rate of effector CD8$^+$ T cells (d^{-1})	(0.5, 0.7) 0.68
δ_{T2}	Number of D_M cells for half-maximal clearance of effector CD8$^+$ T cells	(3.5, 5.5) 3.6
π_{B1}	Maximum activation rate of naive B cells (d^{-1})	(2.5, 3.5) 2.9
π_{B2}	Number of D_M cells for half-maximal activation of naive B cells	(1×10^4, 2.5×10^4) 1.2×10^{-4}
δ_B	Death rate of naive B cells (d^{-1})	(2×10^{-3}, 3×10^{-3}) 2.5×10^{-3}
ρ_{B1}	Maximum proliferation rate of activated B cells (d^{-1})	(0.9, 1.1) 0.92
ρ_{B2}	Number of D_M cells for half-maximal proliferation of activated B cells	(4×10^3, 5×10^3) 4.8×10^3
h	Factor of B-cell activation by CD4$^+$ T cells	(0.7, 0.9) 0.75
δ_{B_A}	Clearance rate of activated B cells (d^{-1})	(0.4, 0.6) 0.60
π_s	Differentiation rate of activated B cells into short-lived antibody-secreting plasma cells (d^{-1})	(0.4, 0.6) 0.51
π_L	Differentiation rate of activated B cells into long-lived antibody-secreting plasma cells (d^{-1})	(0.4, 0.6) 0.44
δ_S	Death rate of short-lived antibody-secreting plasma cells (d^{-1})	(0.01, 0.5) 0.05
δ_L	Death rate of long-lived antibody-secreting plasma cells (d^{-1})	(0.02, 0.03) 0.28×10^{-1}
π_{A_S}	Secretion rate of antibody titer by unit short-lived plasma call (d^{-1})	(0.3, 0.8) 0.67
δ_{A_S}	Clearance rate of short-lived antibody (d^{-1})	(0.05, 0.15) 0.14
π_{A_L}	Secretion rate of antibody titer by unit long-lived plasma call (d^{-1})	(0.3, 0.8) 0.43
δ_{A_L}	Clearance rate of long-lived antibody (d^{-1})	(0.05, 0.15) 0.13

Declaration of competing interest

The authors have no competing interests to declare that are relevant to the content of this article.

Author contributions

Conceptualization, H.H., Y.F.; methodology, H.H., Y.F., X.C.; calibration and validation, H.H.; geometry preparation, E.K., C.F., Y.F., H.H.; simulations, H.H.; data curation, H.H.; data analysis, H.H.; writing, original draft, H.H.; writing, review and editing, H.H., E.K., X.C., Y.F.

Disclaimer

It is not the intention of authors to provide specific medical advice but rather to provide readers with computational modeling details to better understand the fundamentals of fluid dynamics and host cell dynamics in COVID-19 nasal vaccine development. No *in vivo/in vitro* studies were conducted. Hence, no specific medical advice will be provided, and the authors urge you to consult with a qualified physician for answers to your personal medical concerns.

References

Asgharian, B. 2004. A model of deposition of hygroscopic particles in the human lung. *Aerosol Science and Technology*, 38: 938–947.

Baccam, P., Beauchemin, C., Macken, C. A., Hayden, F. G., Perelson, A. S. 2006. Kinetics of influenza A virus infection in humans. *Journal of Virology*, 80: 7590–7599.

Bird, R. B., Stewart, W. E., Lightfoot, E. N., Spalding, D. B. 1960. Transport phenomena. *Journal of Applied Mechanics*, 28: 317–318.

Bleier, B. S., Ramanathan, M., Lane, A. P. 2021. COVID-19 vaccines may not prevent nasal SARS-CoV-2 infection and asymptomatic transmission. *Otolaryngology—Head and Neck Surgery*, 164: 305–307.

清华大学出版社 Tsinghua University Press Springer

Brechtel, F. J., Kreidenweis, S. M. 2000. Predicting particle critical supersaturation from hygroscopic growth measurements in the humidified TDMA. Part I: Theory and sensitivity studies. *Journal of the Atmospheric Sciences*, 57: 1854–1871.

Broday, D. M., Georgopoulos, P. G. 2001. Growth and deposition of hygroscopic particulate matter in the human lungs. *Aerosol Science and Technology*, 34: 144–159.

Butler, S. E., Crowley, A. R., Natarajan, H., Xu, S., Weiner, J. A., Bobak, C. A., Mattox, D. E., Lee, J., Wieland-Alter, W., Connor, R. I., et al. 2021. Distinct features and functions of systemic and mucosal humoral immunity among SARS-CoV-2 convalescent individuals. *Front Immunol*, 11: 618685.

Calmet, H., Inthavong, K., Eguzkitza, B., Lehmkuhl, O., Houzeaux, G., Vázquez, M. 2019. Nasal sprayed particle deposition in a human nasal cavity under different inhalation conditions. *PLoS One*, 14: e0221330.

Chavda, V. P., Vora, L. K., Pandya, A. K., Patravale, V. B. 2021. Intranasal vaccines for SARS-CoV-2: From challenges to potential in COVID-19 management. *Drug Discovery Today*, 26: 2619–2636.

Chen, M., Shen, W., Rowan, N. R., Kulaga, H., Hillel, A., Ramanathan, M. Jr., Lane, A. P. 2020. Elevated ACE-2 expression in the olfactory neuroepithelium: Implications for anosmia and upper respiratory SARS-CoV-2 entry and replication. *European Respiratory Journal*, 56: 2001948.

Chen, X., Feng, Y., Zhong, W., Kleinstreuer, C. 2017. Numerical investigation of the interaction, transport and deposition of multicomponent droplets in a simple mouth-throat model. *Journal of Aerosol Science*, 105: 108–127.

El Golli, S., Bricard, J., Turpin, P. Y., Treiner, C. 1974. The evaporation of saline droplets. *Journal of Aerosol Science*, 5: 273–292.

Ferron, G. A., Upadhyay, S., Zimmermann, R., Karg, E. 2013. Model of the deposition of aerosol particles in the respiratory tract of the rat. II. Hygroscopic particle deposition. *Journal of Aerosol Medicine and Pulmonary Drug Delivery*, 26: 101–119.

Flaherty, S. 2021. Children could be dangerous carriers of virus. Available at https://finchannel.com/children-could-be-dangerous-carriers-of-virus/.

Fleming, S., Thompson, M., Stevens, R., Heneghan, C., Plüddemann, A., Maconochie, I., Tarassenko, L., Mant, D. 2011. Normal ranges of heart rate and respiratory rate in children from birth to 18 years of age: A systematic review of observational studies. *Lancet*, 377: 1011–1018.

Glezen, W. P. 2001. The new nasal spray influenza vaccine. *Journal of Pediatric Infectious Diseases*, 20: 731–732.

Haghnegahdar, A., Zhao, J., Feng, Y. 2019. Lung aerosol dynamics of airborne influenza A virus-laden droplets and the resultant immune system responses: An in silico study. *Journal of Aerosol Science*, 134: 34–55.

Hassan, A. O., Kafai, N. M., Dmitriev, I. P., Fox, J. M., Smith, B. K., Harvey, I. B., Chen, R. E., Winkler, E. S., Wessel, A. W., Case, J. B., et al. 2020. A single-dose intranasal ChAd vaccine protects upper and lower respiratory tracts against SARS-CoV-2. *Cell*, 183: 169–184.

Hayati, H., Feng, Y., Hinsdale, M. 2021. Inter-species variabilities of droplet transport, size change, and deposition in human and rat respiratory systems: An in silico study. *Journal of Aerosol Science*, 154: 105761.

Hayati, H., Soltani Goharrizi, A., Salmanzadeh, M., Ahmadi, G. 2019. Numerical modeling of particle motion and deposiiton in turbulent wavy channel flows. *Scientia Iranica*, 26: 2229–2240.

Hou, Y. J., Okuda, K., Edwards, C. E., Martinez, D. R., Asakura, T., Dinnon, K. H., Kato, T., Lee, R. E., Yount, B. L., Mascenik, T. M., et al. 2020. SARS-CoV-2 reverse genetics reveals a variable infection gradient in the respiratory tract. *Cell*, 182: 429–446.

Inthavong, K., Tian, Z. F., Li, H. F., Tu, J. Y., Yang, W., Xue, C. L., Li, C. G. 2006. A numerical study of spray particle deposition in a human nasal cavity. *Aerosol Science and Technology*, 40: 1034–1045.

Inthavong, K., Tian, Z. F., Tu, J. Y., Yang, W., Xue, C. 2008. Optimising nasal spray parameters for efficient drug delivery using computational fluid dynamics. *Computers in Biology and Medicine*, 38: 713–726.

Kapadia, M., Grullo, P. E. R., Tarabichi, M. 2019. Comparison of short nozzle and long nozzle spray in sinonasal drug delivery: A cadaveric study. *Ear, Nose & Throat Journal*, 98: E97–E103.

Kiaee, M., Wachtel, H., Noga, M. L., Martin, A. R., Finlay, W. H. 2018. Regional deposition of nasal sprays in adults: A wide ranging computational study. *International Journal of Numerical Methods in Biomedical Engineering*, 34: e2968.

Kitaoka, H. 2011. A 4D model generator of the human lung. *Forma*, 26: 19–24.

Kolanjiyil, A. V., Alfaifi, A., Aladwani, G., Golshahi, L., Longest, W. 2022. Importance of spray-wall interaction and post-deposition liquid motion in the transport and delivery of pharmaceutical nasal sprays. *Pharmaceutics*, 14: 956.

Koomen, E., Nijman, J., Nieuwenstein, B., Kappen, T. 2021. Tidal volume in pediatric ventilation: Do You get what you see? *Journal of Clinical Medicine*, 11: 98.

Krammer, F. 2020. SARS-CoV-2 vaccines in development. *Nature*, 586: 516–527.

Kreidenweis, S. M., Koehler, K., DeMott, P. J., Prenni, A. J., Carrico, C., Ervens, B. 2005. Water activity and activation diameters from hygroscopicity data - Part I: Theory and application to inorganic salts. *Atmospheric Chemistry and Physics*, 5: 1357–1370.

Lee, H. Y., Topham, D. J., Park, S. Y., Hollenbaugh, J., Treanor, J., Mosmann, T. R., Jin, X., Ward, B. M., Miao, H., Holden-Wiltse, J., et al. 2009. Simulation and prediction of the adaptive immune response to influenza A virus infection. *Journal of Virology*, 83: 7151–7165.

Li, H., Kuga, K., Khoa, N. D., Ito, K. 2021. Effects of initial conditions and parameters on the prediction of SARS-CoV-2 viral load in the upper respiratory tract based on host-cell dynamics. In: Proceedings of International Exchange and Innovation Conference on Engineering & Science Interdisciplinary Graduate School of Engineering Sciences, 7: 155–160.

Long, Q. X., Liu, B. Z., Deng, H. J., Wu, G. C., Deng, K., Chen, Y. K., Liao, P., Qiu, J. F., Lin, Y., Cai, X. F., et al. 2020. Antibody responses to SARS-CoV-2 in patients with COVID-19. *Nature Medicine*, 26: 845–848.

Longest, P. W., Xi, J. 2008. Condensational growth may contribute to the enhanced deposition of cigarette smoke particles in the upper respiratory tract. *Aerosol Science and Technology*, 42: 579–602.

Menter, F. R., Langtry, R. B., Likki, S. R., Suzen, Y. B., Huang, P. G., Völker, S. 2006. A correlation-based transition model using local variables—Part I: Model formulation. *Journal of Turbomachinery*, 128: 413.

Moakes, R. J. A., Davies, S. P., Stamataki, Z., Grover, L. M. 2021. Formulation of a composite nasal spray enabling enhanced surface coverage and prophylaxis of SARS-COV-2. *Advanced Materials*, 33: e2008304.

Morrison, N. A., Talashek, T. A., Yu, H., Raczkowski, R. 2020. Gellan gum products and methods of manufacture and use thereof. U.S. Patent No. 10,638,783. Washington, DC: U.S. Patent and Trademark Office.

Pan, Y., Zhang, D., Yang, P., Poon, L. L. M., Wang, Q. 2020. Viral load of SARS-CoV-2 in clinical samples. *The Lancet Infectious Diseases*, 20: 411–412.

Parham, P. 2014. *The Immune System*. USA: Garland Science.

Pawelek, K. A., Dor, D., Salmeron, C., Handel, A. 2016. Within-host models of high and low pathogenic influenza virus infections: The role of macrophages. *PLoS One*, 11: e0150568.

Perry, R. H., Green, D. W., Maloney, J. O. 1984. *Perry's Chemical Engineers' Handbook*. New York: McGraw-Hill.

Pilicheva, B., Boyuklieva, R. 2021. Can the nasal cavity help tackle COVID-19? *Pharmaceutics*, 13: 1612.

Rygg, A., Hindle, M., Longest, P. W. 2016. Linking suspension nasal spray drug deposition patterns to pharmacokinetic profiles: A proof-of-concept study using computational fluid dynamics. *Journal of Pharmaceutical Sciences*, 105: 1995–2004.

Saffman, P. G. 1965. The lift on a small sphere in a slow shear flow. *Journal of Fluid Mechanics*, 22: 385–400.

Sungnak, W., Huang N., Bécavin C., Berg M., Queen R., Litvinukova M., Talavera-López C., Maatz H., Reichart D., Sampaziotis F., et al. 2020. SARS-CoV-2 entry factors are highly expressed in nasal epithelial cells together with innate immune genes. *Nature Medicine*, 26: 681–687.

Tong, X., Dong, J., Shang, Y., Inthavong, K., Tu, J. 2016. Effects of nasal drug delivery device and its orientation on sprayed particle deposition in a realistic human nasal cavity. *Computers in Biology and Medicine*, 77: 40–48.

Vaidya, N. K., Bloomquist, A., Perelson, A. S. 2021. Modeling within-host dynamics of SARS-CoV-2 infection: A case study in ferrets. *Viruses*, 13: 1635.

Whitaker, S. 1972. Forced convection heat transfer correlations for flow in pipes, past flat plates, single cylinders, single spheres, and for flow in packed beds and tube bundles. *AIChE Journal*, 18: 361–371.

Xi, J., Lei, L. R., Zouzas, W., April Si, X. 2021. Nasally inhaled therapeutics and vaccination for COVID-19: Developments and challenges. *MedComm*, 2: 569–586.

Zare, F., Aalaei, E., Zare, F., Faramarzi, M., Kamali, R. 2022. Targeted drug delivery to the inferior meatus cavity of the nasal airway using a nasal spray device with angled tip. *Computer Methods and Programs Biomedicine*, 221: 106864.